Radio frequency radiation beam pattern of lightning return strokes: Inferred from FORTE satellite observations

Xuan-Min Shao, Abram R. Jacobson, and T. Joseph Fitzgerald

Space and Remote Sensing Sciences Group, Los Alamos National Laboratory, Los Alamos, New Mexico, USA

Received 22 March 2005; revised 23 July 2005; accepted 6 October 2005; published 17 December 2005.

[1] The fast propagating return stroke is expected to produce a radiation pattern differing from a dipole pattern, with a "correction" of $(1 - v \cos \theta/c)^{-1}$ or the so-called F factor. The FORTE satellite measures lightning Very High Frequency (VHF) radiation at different angles from the up space and offers the first opportunity of examining the F factor. In this report, we studied a group of FORTE-detected lightning events that were also observed by the National Lightning Detection Network (NLDN). NLDN provided the discharges' geolocations and helped to identify the discharge types. During the summers of 1998 and 1999, 25,721 coincident events were found. Among these, 2092 were found to be narrow (<100 ns), VHF-intense and highly polarized bursts and were found to be associated with the beginning of return strokes. Through careful statistical analysis regarding the distributions of the event occurrence, we found that the overall ensemble of events can be considered to have an isotropic pattern in the upper half-space. The subset of the narrow bursts displays a beam pattern that agrees with the F factor at a propagating speed of $v = 0.75c$. The latter is inferred by comparing FORTE observations to a free-space transmission line (TL) model. The analysis shows that the ground does not affect the narrow-burst beam pattern observed from the upper half-space; the source for the narrow burst needs to be a few tens of meters above the surface of the Earth and is apparently associated with the junction point of the attachment process. The physical size of the corresponding discharge is estimated to be less than 20 m. The analysis also suggests that a single upward current is responsible for the observations, rather than a bidirectional current as suggested by others for the attachment process. Similarly, the traveling current source (TCS) model that consists of a simultaneous downward current is found less suitable for the initiation of return strokes.

Citation: Shao, X.-M., A. R. Jacobson, and T. J. Fitzgerald (2005), Radio frequency radiation beam pattern of lightning return strokes: Inferred from FORTE satellite observations, *J. Geophys. Res.*, *110*, D24102, doi:10.1029/2005JD006010.

1. Introduction

[2] Return strokes that follow a transmission line (TL) model [e.g., *Uman and McLain*, 1969] have been shown to produce a radiation beam pattern of $\sin \theta(1 - v \cos \theta/c)^{-1}$ [e.g., *Le Vine and Willett*, 1992; *Thottappillil et al.*, 1998], where θ is the viewing angle referenced to the lightning channel, v is the speed of the current wave, and c is the speed of light. The term $(1 - v \cos \theta/c)^{-1}$ is called the F factor and is a "correction" to the dipole pattern $\sin \theta$. When a perfect conducting ground is placed at the base of a vertical channel, the beam pattern becomes $2 \sin \theta[1 - (v \cos \theta/c)^2]^{-1}$ [*Krider*, 1992]. Recently, *Shao et al.* [2004] showed that the F factor is a fundamental factor when a traveling current pulse is considered, and on the basis of this, *Shao et al.* [2005] further derived analytical solutions for the TL, the traveling current source (TCS), and the modified transmission line (MTL) models.

[3] It is clear that the beam pattern mentioned here is for linearly polarized radiation, because of the straight propagation of the current. Unpolarized radiation would simply have an isotropic pattern that involves no directivity. At very low frequency (3–30 kHz) and low frequency (30–300 kHz) (VLF/LF), the corresponding discharge current is constrained along the lightning channel, and the polarization is well justified.

[4] The FORTE satellite detects lightning radiation at very high frequencies (30–300 MHz, VHF) range. At these frequencies the radiation is believed to be associated with small-scale breakdown processes, which may or may not follow a single straight path at any given time. It was found [*Shao and Jacobson*, 2002] that VHF radiation produced by common lightning processes like dart and stepped leaders, K-type events, and return strokes is usually unpolarized, indicating that the discharge as viewed at VHF is an ensemble of randomly directed, incoherent breakdown processes. In this case, no angularly dependent radiation pattern is expected.

[5] Nevertheless, a group of narrow bursts that are associated with return strokes [*Jacobson and Shao*, 2002]

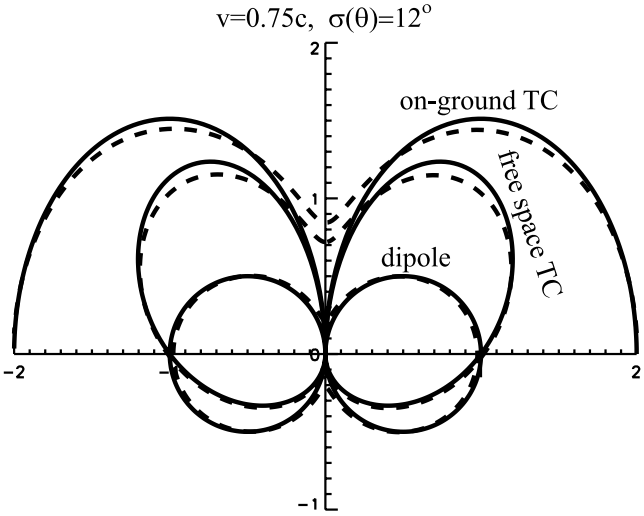

Figure 1. Theoretical beam patterns of radiation E field for (1) free-space dipole (sin θ), (2) free-space traveling current pulse (sin θ/[1 − v cos θ/c]), and (3) on-ground traveling current pulse (2 sin θ/[1 − (v cos θ/c)^2]). Solid curves are for purely vertical channels; dashed curves are for channels that are expected to be vertical but may statistically deviate from the vertical by a certain extent (σ(θ) = 12°). The speed v for the traveling current is assumed 0.75c.

was found to be highly linearly polarized, and therefore the corresponding current must traverse a unique, straight path. For these events, one would expect to see the directional effects on the radiation intensity. *Jacobson and Shao* [2002] found that ~10% of the FORTE-detected return strokes were associated with such narrow bursts, and a majority of them were over seawater. This type of discharge is expected to be oriented nearly vertically, especially when they occur over flat and electrically uniform seawater. Since the FORTE position is known for each event, if the terrestrial location for such a return stroke is provided, the viewing angle to its channel can be computed. Therefore one might hope to detect the beam pattern via such an observation.

[6] However, FORTE only probes an event from a single angle and cannot give the angle-dependent beam pattern for the individual event. Fortunately, thousands of such strokes had been observed by FORTE and at the same time were geolocated by the United States National Lightning Detection Network (NLDN), during the summers of 1998 and 1999. If all the strokes are grouped together, FORTE views the group from all possible angles from the upper half-space. This situation offers us a unique opportunity of examining the directional characteristics of the radiation due to the fast traveling current wave.

2. Statistically Averaged Beam Pattern

[7] *Shao et al.* [2004] presented the radiation field as

$$d\boldsymbol{E} = \frac{1}{4\pi\varepsilon_0 c^2}\frac{1}{r}\frac{\sin\theta}{(1 - v\cos\theta/c)}\frac{\partial i(z', t')}{\partial t'}dz'\hat{\boldsymbol{a}}_{\boldsymbol{\theta}} \qquad (1)$$

for a current pulse traveling in free space without any ground effect, and

$$d\boldsymbol{E} = \frac{2}{4\pi\varepsilon_0 c^2 r}\frac{\sin\theta}{\left(1 - (v\cos\theta/c)^2\right)}\frac{\partial i(z', t')}{\partial t'}dz'\hat{\boldsymbol{a}}_{\boldsymbol{\theta}} \qquad (2)$$

for a current pulse traveling vertically right above the surface of the Earth. These equations are for an individual event. As discussed below, our analysis will instead deal with the statistics of groups of events. For the return strokes that occurred over seawater and started with a narrow, linearly polarized VHF burst, the channel (at least the lower portion) can be assumed nearly vertical. Statistically, as a group, they could be considered to have an average vertical orientation with each individual stroke aligning in different directions in the upper half-space. Using equations (1) and (2) and assuming a Gaussian directional distribution with a standard derivation of 12° from the vertical, the statistically averaged beam patterns for (1) a dipole (v = 0, equation (1)), (2) a traveling current pulse in free space (v = 0.75c, equation (1)), and (3) a traveling current pulse just above the ground (v = 0.75c, equation (2)) are illustrated by the dashed curves in Figure 1. The solid curves show the corresponding beam patterns with purely vertical current movement. It can be seen that for the dipole pattern, there is not much change. For the traveling current cases in free space and on the ground, the overhead nulls are somewhat filled in, but there is no significant change in the rest of the patterns. The statistically averaged beam patterns will be used later in the analysis.

3. FORTE/NLDN Joint Observations

[8] The FORTE satellite was launched into a 70° inclination, circular orbit at 800 km altitude on 29 August 1997. It carries a pair of linear polarization, log periodic dipole array antennas (LPA) that have a primary frequency coverage between 30 and 90 MHz. The RF payload includes a pair of broadband receivers with analog bandwidths of 22 MHz. Each receiver's output, in the form of electric field E, is digitized at a rate of 50 megasamples per second with 12-bit resolution. For studies presented in this paper, the receivers (or at least one of the two) were tuned to 26–48 MHz. An 8-channel subband trigger system was used to trigger the FORTE data recording system, which was designed to overcome the typically overwhelming man-made signals over the analog passband. More detailed and complete descriptions of the FORTE RF payload and its performance have been presented by *Jacobson et al.* [1999] and *Jacobson and Shao* [2002]. Further discussion on the trigger system will be presented later in this paper.

[9] During the summers of 1998 and 1999, collaborative observations between FORTE and NLDN were conducted. NLDN is an array of VLF-LF sensors that covers lightning discharges (mostly cloud-to-ground discharges) throughout the continental United States [*Cummins et al.*, 1998]. The NLDN data were specially postprocessed in a relaxed criterion mode to maximize the detection range for cloud-to-ground (CG) discharges and to include possible in-cloud (IC) discharges. For each detected event, NLDN provided information on the type of the discharge (e.g., IC, −CG, +CG), the location, and the inferred peak current. During the two summers, 25,721 coincidences were obtained between FORTE and NLDN. The method for establishing

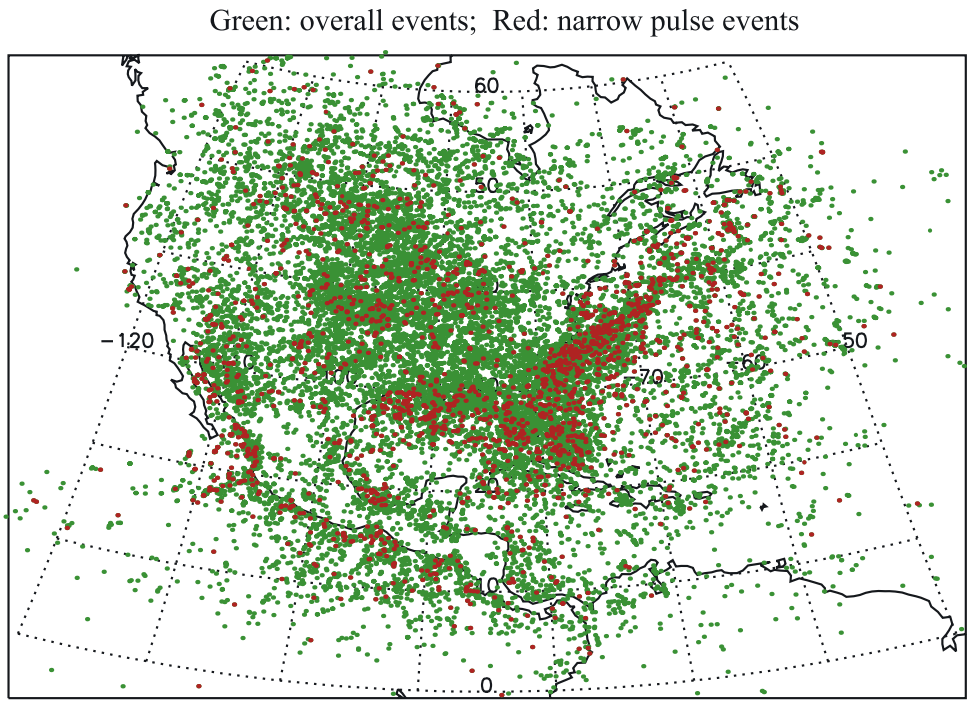

Figure 2. Geographic locations of FORTE/NLDN coincident events. Green dots are for the overall events; red dots are for the very narrow, return stroke-initiating events.

the coincidence and for characterizing its reliability was described by *Jacobson et al.* [2000].

[10] Figure 2 maps all the FORTE/NLDN coincident events (green) over the continental US and the surrounding regions. The red dots indicate the ground strokes that were associated with a very narrow VHF burst, as will be further discussed later. Among all the events, 10,763 are −CGs, 5386 are +CGs, 2173 are ICs, and the remaining 7397 are undetermined polarity ground strokes (G), as previously reported by *Jacobson and Shao* [2002]. The last category is due to distant strokes that occurred 625 km or farther from the nearest NLDN sensor. The fractions for different types of discharges mentioned here should not be confused with their natural occurrence. The two monitoring systems are sensitive to different portions of the radio spectrum, with NLDN being designed primarily for detection of CGs and FORTE for detection of VHF radiation that can be equally produced by CGs and ICs. The rate of coincidence for a specific event type is affected by the different detection biases of the two systems.

[11] For this study, NLDN provided the necessary information on the discharge's location and type. Since the position of FORTE is known for each event, the satellite discharge viewing angle can be derived, as illustrated in Figure 3. In addition, if the discharge type is labeled as a CG by NLDN, in which case the channel is expected to be nearly vertical, the probing angle to the channel (zenith angle, θ), can be obtained. This provides the necessary foundation for the beam pattern examination.

4. Analysis

[12] In this section we will perform a series of extensive but necessary analyses that will lead to the final beam pattern result. First, the VHF burst width and peak power for all the events will be examined, and a group of narrow (<100 ns), polarized events will be extracted from the overall set of events. Distribution of event density as a function of viewing angle (θ) will be computed for both the overall and the narrow-burst events. FORTE's trigger threshold settings and the receiving antennas, both of which affect directly the beam pattern study, will be discussed. On the basis of the observations, a model for the lightning radiation amplitude distribution will be inferred. Putting all these together, we then establish an analytical relation between the lightning beam pattern and the observational

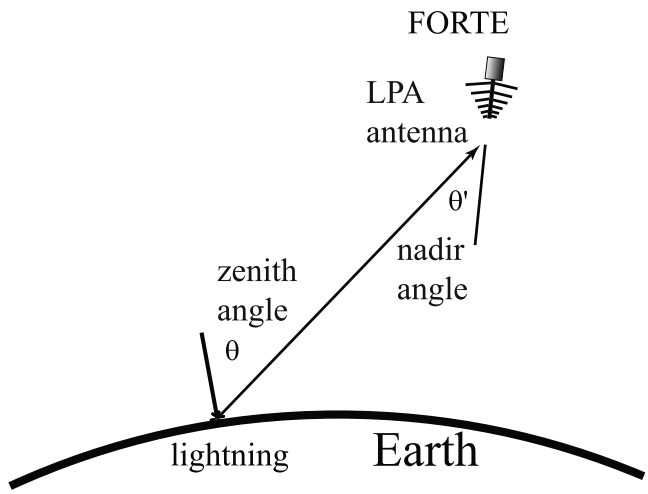

Figure 3. Geometry of the terrestrial lightning and the FORTE satellite. FORTE's LPA antenna points to the center of the Earth.

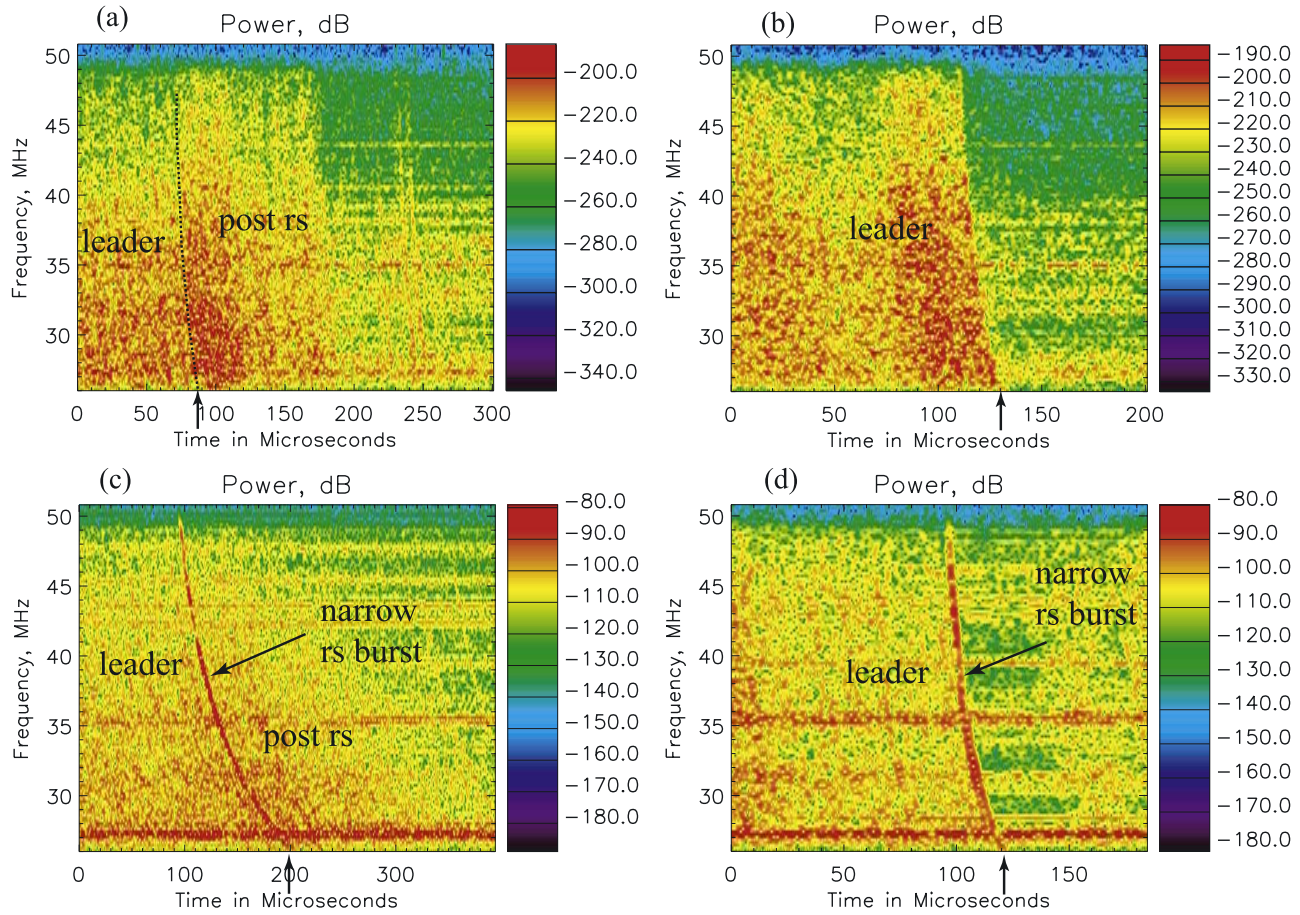

Figure 4. FORTE VHF observations of (a) a "normal" initial stroke, (b) a "normal" subsequent stroke, (c) an initial stroke started with a narrow burst, and (d) a subsequent stroke started with a narrow burst. Time of return stroke is marked by an arrow at 26 MHz. The chirped features are due to transionospheric propagation, and the radiation along the chirped curve would have arrived at the same time without the ionosphere. Different data lengths are chosen to highlight each return stroke, and time zero is arbitrary.

parameters. Finally, possible beam patterns for the overall events and the narrow-burst events will be discussed.

4.1. VHF Burst Width Examination

[13] In the frequency range 26–48 MHz, a transionospheric signal will be chirped (i.e., dispersed) significantly by the ionosphere, such that the highest-frequency component arrives at the satellite first and the rest of the signal is increasingly delayed as frequency decreases. To first order, the group delay is proportional to $1/f^2$, where f is the signal frequency [*Jacobson et al.*, 1999; *Massey et al.*, 1998; *Shao and Jacobson*, 2001]. Figure 4 shows radiation intensity around four different return strokes in the form of spectrograms. The spectrograms were obtained from the time series of the original E field data with a sliding Fourier transform. In the spectrograms, the nature of the dispersion is clearly depicted by the curved features. Without the ionosphere (e.g., for observations on the ground), the different frequency components of an impulsive signal would have arrived at the receiver at the same time, and an impulse would have appeared as vertical in the spectrogram.

[14] Figure 4 shows examples for a "normal" initial −CG stroke (Figure 4a), a "normal" subsequent stroke (Figure 4b), an initial stroke with a distinct radiation burst (Figure 4c), and a subsequent stroke with a distinct radiation burst (Figure 4d). Radiation associated with the leader process, return stroke, and postreturn stroke activity is marked separately in Figure 4. In this study, the stroke type was first categorized with the help of the coincident NLDN observation. A coincidence was selected when the time separation (corrected to the stoke location) was within ±300 μs between the FORTE and NLDN events [*Jacobson et al.*, 2000]. In addition, VHF features of return strokes that were previously observed on the ground were used to further identify the initiation of the return strokes. For an initial stroke the radiation is enhanced at the beginning of the return stroke, and for a subsequent stroke that starts with a dart leader the radiation becomes abruptly quiet after the leader reaches the ground, as reported by *Rhodes et al.* [1994], *Shao et al.* [1995] with narrowband VHF interferometer observations, and by *Shao et al.* [1996, 1999] with broadband VHF observations. On the basis of the ground observations, *Suszcynsky et al.* [2000] were able to identify the different lightning types observed by FORTE.

[15] In Figure 4, the start of the return strokes is marked by an arrow at the lowest frequency. Readers will notice that

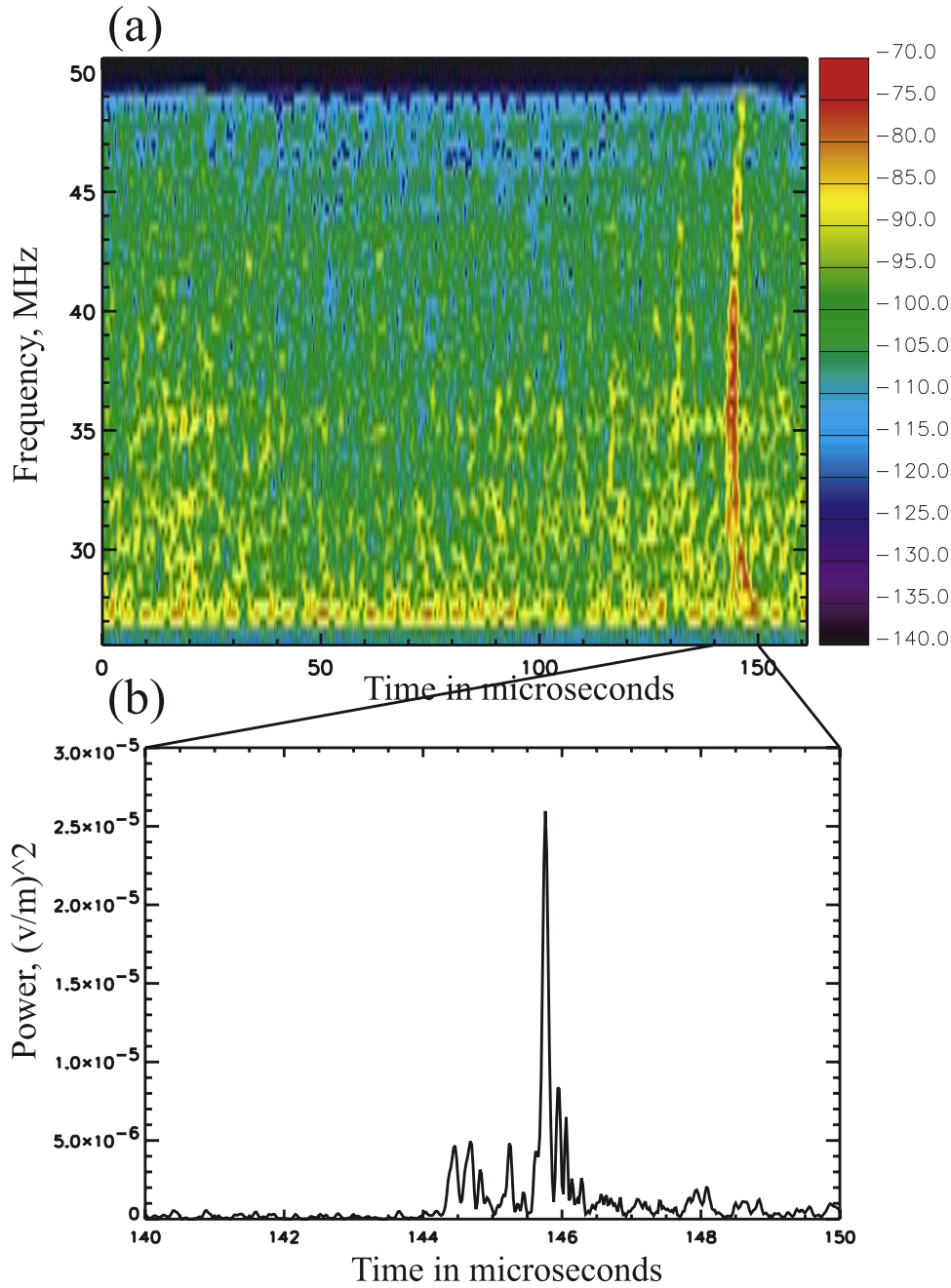

Figure 5. (a) Burst in Figure 4c after matched-filtering deconvolution. Only portion of data is shown to highlight the burst, and time zero is arbitrary. Radiation preceding the burst is associated with leader process. (b) Fine time waveforms of the radiation power around the burst.

the higher-frequency components for the same activity arrived earlier in time. As in the ground observations, for the "normal" initial stroke in Figure 4a, the radiation is enhanced after the start of the return stroke. For the "normal" subsequent stroke in Figure 4b, the radiation became quiet at the time of the return stroke. For strokes with a distinct narrow burst such as the two illustrated in Figures 4c and 4d it was found that the burst occurred systematically within 10 μs of NLDN stroke (mostly −CGs) time, after correction for all known propagation delays [*Jacobson and Shao*, 2002]. On the basis of the FORTE/NLDN time coincidence, the VHF features, and results of other researchers' ground observations of return stroke electric field changes, *Jacobson and Shao* [2002] inferred that the VHF bursts like that shown in Figures 4c and 4d were associated with the initiation of the return strokes, and the 10-μs uncertainty relative to NLDN stroke time was mostly due to the FORTE position and time-stamping errors.

[16] As discussed above, a transionospheric signal at VHF will be chirped by the ionosphere. To recover the "true" burst in the time domain, a "dechirping" method that utilizes a matched-filtering technique is implemented in this study. Through the Earth's ionosphere, the extra

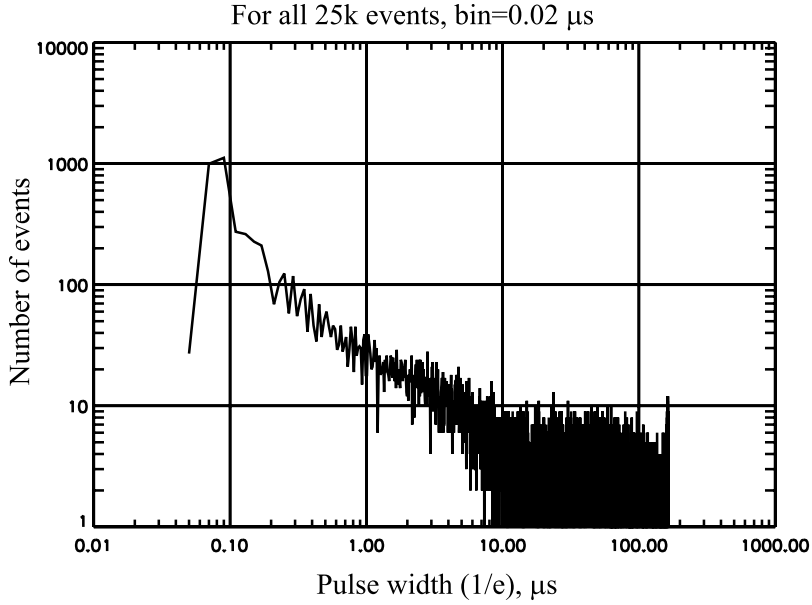

Figure 6. Burst width (1/*e* of peak power) distribution for all the coincident events. Bursts narrower than 100 ns are classed as narrow bursts in this study.

phase delay for a VHF signal can be approximated as (see Appendix A)

$$\int \left(d\varphi_{free\_space} - d\varphi_{ionosphere} \right) = \frac{e^2}{2c\varepsilon_0 m_e} \frac{TEC}{f \pm f_c \cos\gamma} \quad (3)$$

Here, *TEC* is the total electron content integrated along the line of sight; f is the radio frequency (in our case 26–48 MHz); f_c is the electron cyclotron frequency; γ is the angle between the line-of-sight and the Earth's magnetic field; and $\pm$ represents the "ordinary" (O) and "extraordinary" (X) modes of the transionospheric signal. This represents the phase response of the ionospheric matched filter. At VHF, the amplitude response can be assumed unity and frequency-independent.

[17] All the 25,721 coincident events were deconvolved with this matched filter to recover their "true" signatures. In this process, the ordinary mode was matched and the extraordinary mode was ignored. Because of the magnetic splitting through the ionosphere, the two modes have a relative time delay proportional to $1/f^3$ [*Shao and Jacobson*, 2001; *Jacobson and Shao*, 2002]. Dechirping the ordinary mode will still leave the extraordinary mode dispersive and its radiation energy is still stretched in a long time interval. Therefore its peak power measured in the time domain is negligible compared to that of the dechirped ordinary mode, as has been shown by *Jacobson and Shao* [2002, Figures 3 and 5]. In this section, the peak power and burst width are referred to the dechirped ordinary mode.

[18] To do the deconvolution, a section of 8192 points ($\sim$164 μs) was chosen from each FORTE record (time series electric field data), with 1/4 and 3/4 of the points before and after the trigger position. The deconvolution was first carried out in the frequency domain according to equation (3) after a Fourier transformation of the original time series E field data, and was then converted back to the E field in the time domain. In the time domain, the signal's power was computed by summing the squares of the deconvolved data and the Hilbert transform of the deconvolved data. The two parts of the summation correspond to the real and imaginary parts of a complex signal. The Hilbert transform of the real data sequence provided the necessary imaginary sequence for the power calculation [*Stearns and Hush*, 1990]. The peak power in this section was picked out and any point that exceeded 1/*e* of the peak power, or "high point," was marked. The time width between the first and the last occurrences of the high points were stored to represent the apparent width of the radiation burst. The ratio of the peak to the width is used to measure the quality of the burst. This same process was repeated many times with changes of *TEC* value. The highest burst quality among the trials was then selected, and the corresponding peak power and 1/*e* burst width were recorded as the representative characteristics for the specific event. The resultant *TEC* value for each event was compared to the corresponding value determined previously with other techniques [e.g., *Jacobson et al.*, 2000] to assure its validity. Obviously, for a single burst well above the background radiation level (Figures 4c and 4d) the estimated burst width would reflect the true width (through the 22 MHz bandpass filter) and the measured burst quality would be high; whereas for a sequence of erratic signals (Figures 4a and 4b) the apparent "burst" could be as long as the data section itself and the selected peak may not be associated exactly with the return stroke process. In the latter case the burst quality would be low, and as will be discussed later, such a process tends to be unpolarized. In this process, $f_c \cos\gamma$ was obtained with the International Geomagnetic Reference Field (IGRF) model [*Langel*, 1992], and the value at the interception point between the line of sight and the effective height of the ionosphere ($\sim$400 km) was used.

[19] Figure 5 demonstrates the deconvolved burst from the original burst in Figure 4c. In Figure 5a, the output is

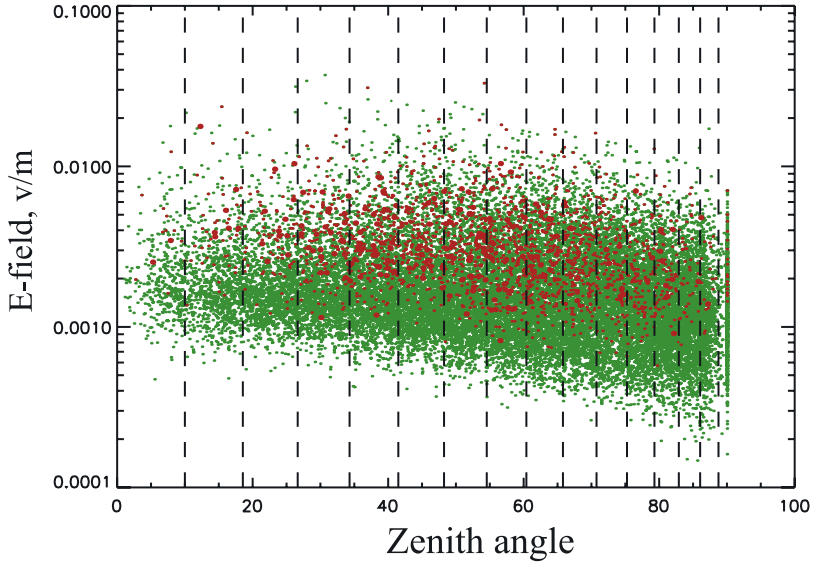

Figure 7. Peak radiation amplitudes (E) for all the coincident events (green) and the narrow bursts (red), as functions of the zenith angle (Figure 3).

shown in a familiar spectrogram format, while in Figure 5b, the time waveform of the power is shown in a much finer, 10 μs interval around the peak. The 1/e width is estimated to be 80 ns.

[20] Figure 6 shows the distribution of the estimated burst width for all the 25,721 events. The minimum width that is physically meaningful should be no less than 60 ns because of the FORTE sampling interval of 20 ns. The maximum width is due to the length of the data segment, which was chosen to be ~164 μs. Interestingly, a clear peak can be seen at the widths narrower than 100 ns. These narrow bursts (total of 2092) were also found to be exclusively associated with return strokes, and are mostly (>90%) associated with negative strokes. The geolocations of the narrow-burst strokes are shown in Figure 2 by the red dots. As previously reported by *Jacobson and Shao* [2002], these strokes are more likely to occur over seawater than over land, not only by the total numbers but also by the respective percentages of such strokes over the overall events within each of the two areas.

4.2. Peak E Field and Number of Events, as Function of Viewing Angle

[21] As illustrated in Figure 3, FORTE viewed each discharge from a known angle. With thousands of such observations, FORTE effectively viewed the discharges from a wide range of possible angles in the upper half-space. Specifically, for return strokes, if the channels can be assumed vertical, the ensemble of the FORTE observations would view the channels from all the different elevation angles, necessary for beam pattern analysis.

[22] This study would be easier if all the return strokes were identical in terms of VHF radiation, as a "standard candle," so that the associated beam pattern could be measured directly. Unfortunately, this is not the case. Figure 7 shows the peak amplitude after being dechirped, as a function of the zenith angle θ (viewed from the discharge to the satellite, Figure 3). In the rest of this paper, we examine the radiation at amplitude rather than at power since (1) the modeled beam pattern in Figure 1 and (2) FORTE's receiving antenna pattern (to be discussed later) are both formulated for radiation amplitude. The peak amplitude is simply the square root of the peak power. In Figure 7, the scatter in |E| at a fixed θ implies scatter in the radiation intensity at the source, since at any given θ the satellite-lightning distance is the same and the range loss is the same. The wide scatter of the radiation amplitude due to the nature of lightning makes the direct beam pattern examination difficult, if not impossible. In addition, the general downward trend of the peak amplitude along increasing zenith angle indicates some other effects (e.g., noise-riding threshold) will also make the direct examination of the beam pattern difficult.

[23] As was mentioned by *Jacobson and Shao* [2002], the event distribution of the narrow-burst strokes, as referred to the viewing angle, is different than that of the overall −CG events. For the present study, we examine this issue further. We split the 90° range of zenith angles into 15 bins as indicated by the dashed lines in Figure 7, with the first bin covering 0–10° and the last bin covering 86.1–88.8°, the bin sizes in between decreasing linearly. This bin selection partially accommodates the uneven event distribution (Figure 7) and yet gives a reasonable angular resolution. We summed the number of events within each bin and computed the corresponding area on the surface of the Earth associated with each bin. The event number was then divided by the surface area, giving the event density normalized to a unit area. Figure 8 shows the density distributions for the overall set of events (solid line) and the narrow-burst events (dashed line), which were separately normalized to their respective maxima. It is clear that the subset of the narrow-burst strokes displays a significantly different distribution compared to that of the overall events. In the case of a single radiator and simultaneous all-sky observation, this density distribution is statistically equivalent to the detection probability of the same radiator at different zenith angles. Considering that the detection probability must be related to the radiation

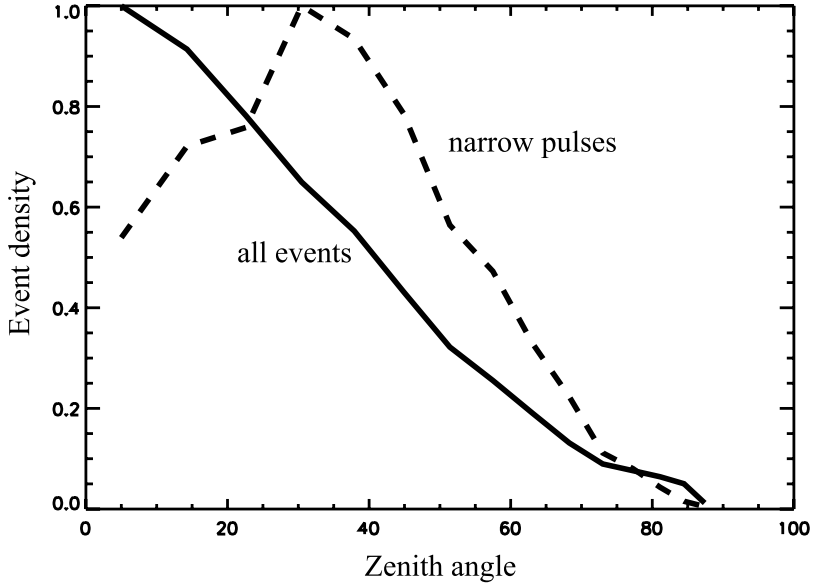

Figure 8. Distributions of area-normalized number of events (event density), at the angular bins shown in Figure 7. Solid curve is for the overall events and dashed curve is for the narrow bursts. Each curve is normalized to its maximum for comparison.

intensity, Figure 8 suggests that there are different radiation beam patterns for the two different groups of discharges.

4.3. FORTE Trigger Threshold

[24] To investigate the event density shown in Figure 8, the FORTE trigger mechanism needs to be described and examined. FORTE is triggered by an 8-channel subband system. Each subband is 1 MHz wide, and the eight subbands are evenly placed in 26–48 MHz. A trigger is generated if 5 out of the 8 subbands detect a signal that is above the precommanded threshold, within a certain time interval (162 μs) to accommodate ionospheric dispersion. The threshold is either set at an absolute value or at a relative value above an averaged noise level. The latter, "noise riding threshold" was used during almost all the lightning observations, and the relative level was typically set 14–20 dB above the noise level at each subband.

[25] The background noise at each subband was first measured and averaged within a 2 ms interval about each second. The mean of 8 such noise measurements was then registered and updated every second as the current noise level for the specific subband. The noise level, as well as the actual threshold at each subband was recorded in FORTE's State of Health (SOH) file in the form of E field amplitude, but were only sampled every 8 s. These features introduce uncertainties between the SOH-reported and the actual threshold level at each subband for a specific event.

[26] To retrieve an approximate trigger threshold for each event, we extracted from the SOH the threshold value that is nearest in time to the event. In theory, the time of the extracted threshold could be as far as 4 s away from the time the event was triggered. Among the 8 subband thresholds, the mean of the lowest five was estimated and was used to represent the possible threshold for the specific event. Figure 9 shows the possible thresholds for all the FORTE/NLDN coincident events, in the same format as Figure 7.

[27] It is clear that an accurate threshold level for each specific FORTE lightning event cannot be obtained. The inferred threshold is rather an approximation that may randomly occur in a certain range. Fortunately, the exact threshold is not absolutely necessary for the beam pattern analysis. As described above, because of the random nature of the lightning radiation intensity itself, the beam pattern will have to be examined by looking into the statistical properties of the event density distribution, or the detection probability. The threshold itself can be treated as another random parameter in the statistical process, as will be discussed later.

[28] Figure 9 shows that at any given zenith angle, the inferred threshold can vary over a large range. This is primarily due to the possibility that each event at the same angle could be associated with a different storm that may occur in a different region at a different time under a different satellite pass, so that the associated noise level (and the threshold) would be independent from each other. It should be noticed that the thresholds for the narrow-burst events (red dots in Figure 9) display the same random spread as that of the overall events. This is expected since the threshold was determined by the temporally smoothed background noise but not by the impulsive lightning radiation.

[29] As a function of the zenith angle, it is interesting to note that the inferred threshold values display a general downward trend. In an ideal, globally uniform noise environment, the noise background should have had been more or less the same no matter where the satellite was. Although the trigger threshold displays a similar trend as that of the lightning radiation amplitude, the lightning activity should have little effect on the noise level, since (1) the duty cycle of the lightning VHF radiation is very low and (2) on top of that the duty cycle of the noise sampling by FORTE is also very low (2 ms/s). The relative higher threshold/noise at smaller zenith angles is

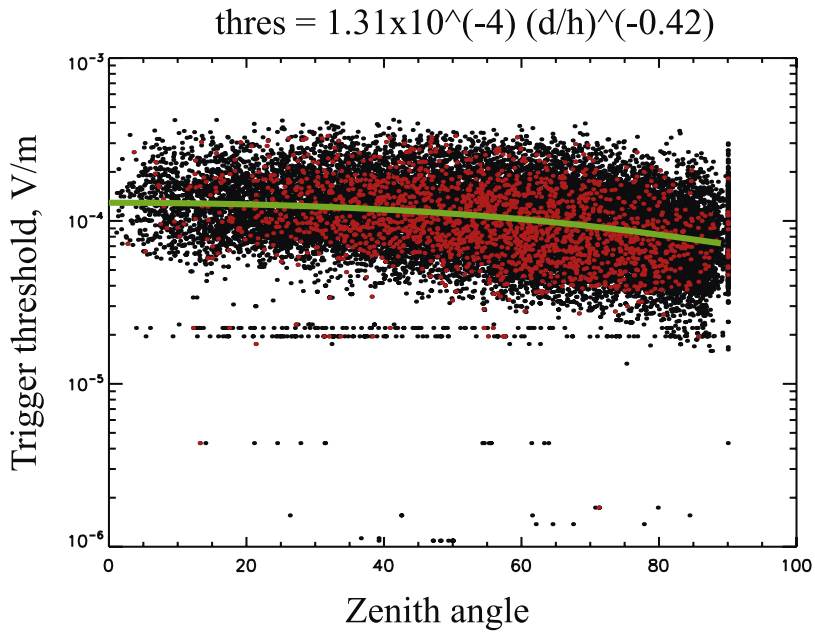

Figure 9. Apparent FORTE trigger threshold for all the coincident events (black dots) and the narrow-burst events (red dots). Green line indicates the best power law fit to the scattered points, $1.31 \times 10^{-4}\ (d/H)^{-0.42}$, where H is the orbit height, 800 km; d is the lightning-satellite distance, a function of zenith angle.

believed to be due to a noisier background over the continental US and neighboring regions.

[30] The green line in Figure 9 shows the best power law fit to the threshold values. Transferring the zenith angle θ to the lightning-satellite distance d, i.e.,

$$d(\theta) = \sqrt{(R_e + H)^2 - R_e^2 \sin^2\theta} - R_e \cos\theta \qquad (4)$$

the green line follows a relation like $(d/H)^{-0.42}$, where H is the height of the FORTE orbit, 800 km; and R_e is the radius of the Earth. This relation will be used later in the beam pattern analysis.

4.4. FORTE Antenna Pattern

[31] Practically, all antennas have a certain directivity that will respond differently to signals incident from different directions. To study the detection probability as a function of the viewing angle, the directional response of the FORTE antenna has to be examined.

[32] FORTE's two linear polarization, log periodic dipole array (LPA) antennas are mounted orthogonal to each other along the same boom that points to the satellite's nadir (center of the Earth). In Figure 3, one LPA antenna is illustrated schematically to facilitate the discussion. The polarization (the dipole elements) of one antenna is aligned with the satellite trajectory (ram) and that the other in the cross-track direction. When the antenna operates at the low end (26–48 MHz) of its primary frequency range (30–90 MHz) its relative directivity/gain can be approximated by 1 in the H plane (perpendicular to the antenna element), and by

$$g'(\alpha') = \frac{\sin(2\pi\alpha'/BW)}{(2\pi\alpha'/BW)} \qquad (5)$$

in the E plane (parallel to the antenna element), as described previously by *Shao and Jacobson* [2001, equation (17)]. Here, BW is the beamwidth between the first nulls, and α' is the angle between the nadir and the line of sight projection in the E plane. In Figure 10a, the antenna element is aligned with y′ and α' is measured in the z′-y′ plane. At 26–48 MHz, BW can be approximated by π. For the cross-track antenna shown in Figure 10a, we have [*Shao and Jacobson*, 2001, equation (10)]

$$\tan\alpha' = \tan\theta' \sin\phi' \qquad (6)$$

where θ' and ϕ' are nadir and azimuthal angles in the satellite's coordinates. As one would expect, at the broadside ($\alpha' = 0$) the antenna has the maximum response, and at the endfire $\alpha' = \pm 90°$ the antenna has the minimum response. At a given θ' around the nadir direction, as indicated by the dotted ellipse (a circle if viewed in the z′ direction) in Figure 10a, the gain follows a locus that can be approximated by an ellipse (the solid ellipse). Numerical solution for equation (5) is shown in Figure 10b, as a function of ϕ' at three given θ' s. It should be noted that the maximum nadir angle from FORTE to the Earth is ∼62°, which corresponds to 90° of zenith angle θ.

[33] Although both θ' and ϕ' can be determined for each FORTE/NLDN coincident event and the radiation amplitude can be corrected with the antenna pattern, for the analysis in this paper, only θ (θ')-dependent observations are considered. First, the beam pattern for a vertical discharge depends only on θ, as shown in Figure 1. Secondly, the event distributions (Figure 8), which will be used later for the statistic beam pattern study, are also a sole function of θ. Thirdly, since the level of the trigger threshold cannot be directly related to the coincident lightning event, its

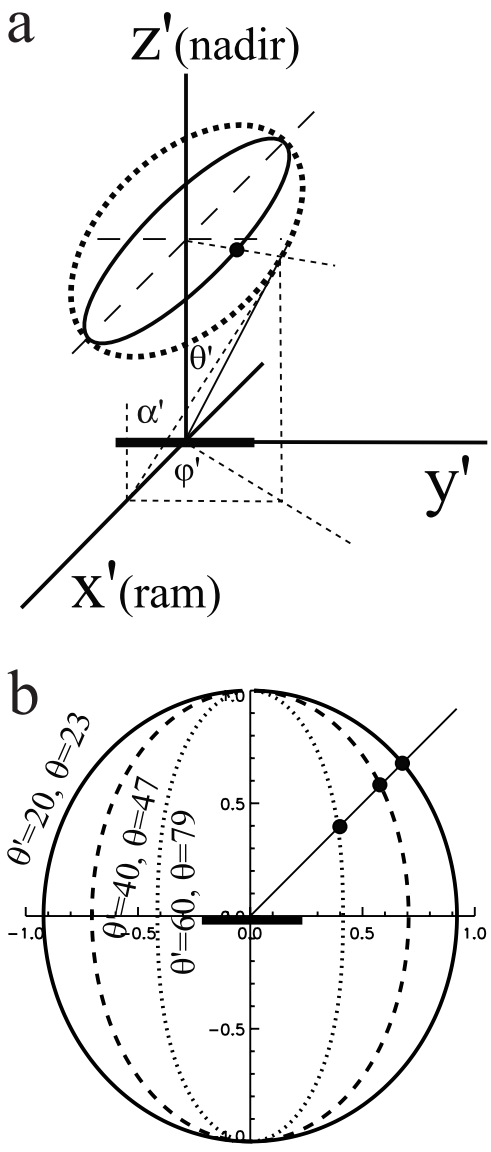

Figure 10. Illustration of antenna response in the satellite coordinates. (a) Thick line represents the cross-track antenna. The dotted ellipse prescribes a circle around the nadir direction at a certain nadir angle, and the solid ellipse indicates the corresponding antenna response. (b) Computed responses as function of ϕ' for three nadir angles θ', according to equations (5) and (6). Here, θ is the corresponding zenith angle from lightning to FORTE. The middle point between the maximum and minimum response is used to approximate the effective response at each nadir angle.

behavior can only be examined statistically along θ' but not along ϕ'. Finally, in the later statistic analysis, exact radiation amplitude for each lightning events is not needed but rather the statistic amplitude distributions.

[34] Therefore an effective antenna response that depends only on θ (θ') is needed. Because of the elliptical pattern in Figure 10b, the effective response at each θ (θ') can be approximated by $\sqrt{g'^2_{\max}(\theta') + g'^2_{\min}(\theta')}/\sqrt{2}$ at the middle point between the maximum and minimum. When $\phi' = 0$, 180° (in front or behind the antenna), from equation (6) we have $\alpha' = 0$. Using equation (5) we can see that the antenna has the maximum gain $g'(0) = 1$ in these two directions. Similarly, when $\phi' = \pm 90°$ we have $\alpha' = \pm\theta'$, and the antenna has the minimum gain $g'(\alpha') = g'(\theta') = \sin(2\pi\theta'/BW)/(2\pi\theta'/BW)$. Therefore the effective response at a certain nadir angle θ' can be solely related to θ' as

$$\bar{g}(\theta') = \frac{1}{\sqrt{2}}\sqrt{1 + [g'(\theta')]^2} \tag{7}$$

It is straightforward to show that the Earth-based zenith angle θ is uniquely related to the satellite-based nadir angle θ' (Figure 3) by

$$\sin\theta = \frac{H + R_e}{R_e}\sin\theta' \tag{8}$$

Using this relation, the effective directivity of the FORTE antenna viewed from the terrestrial lightning, $g(\theta)$, can be readily obtained.

[35] During the two summers, FORTE's VHF trigger circuit was mostly connected to the cross-track antenna. Figure 11 shows that more events were captured at the broadside of the antenna (in front or behind the satellite) than at the endfire (in cross track), apparently because of the antenna directivity discussed above (Figure 10).

4.5. Probability of FORTE Detection of a Lightning Event

[36] For FORTE to record a lightning event, the event's radiation amplitude must exceed the trigger threshold. To study the probability of an event that meets this condition, the possible radiation amplitude the event may produce, or in other words, the amplitude distribution, needs to be examined.

[37] To estimate the true amplitude the different range losses ($1/d$) need to be considered. The distance d and zenith angle θ follows the relation of equation (4). Figure 12a shows the range-corrected peak amplitudes for both the overall (black dots) and narrow-burst events (red dots), and the downward trend in Figure 7 is roughly rectified. All the amplitudes were normalized to 100 km, a distance commonly used by lightning researchers for radiation amplitude comparison. Comparison between FORTE's narrow-burst amplitude to previous ground-based LF-HF observations had been discussed by *Jacobson and Shao* [2002].

[38] Figure 12b shows the amplitude distributions for the two groups. Beyond 0.02 V/m, both distributions follow the same rate of decline with increasing amplitude. The peak for the overall events occurs near 0.01 V/m, indicating the minimum trigger level of the receiver. The peak for the narrow-burst events is near 0.02 V/m and the peak is broadened. The slight difference near the peak areas is likely due to the selection process for the narrow bursts. As discussed in section 4.1, a narrow burst was identified only if its peak was above the surrounding radiation level. For a week burst that is embedded among other radiation, it would less likely be identified.

[39] Beyond 0.02 V/m the trigger threshold and peak identification process will no longer affect the distributions

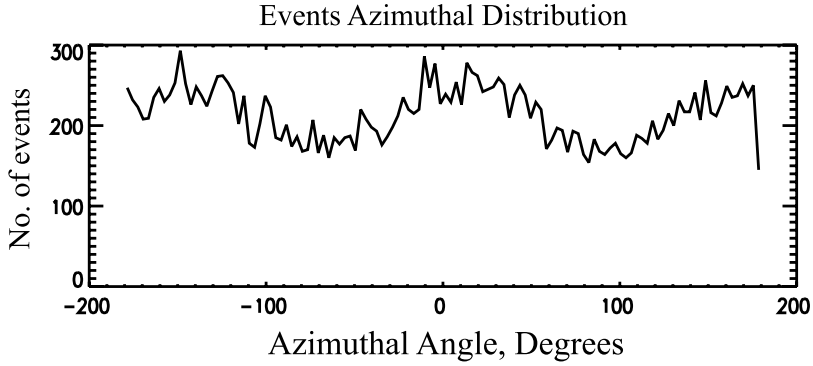

Figure 11. Event distribution around the azimuth as viewed from the satellite. More events were triggered in the ram direction than in the cross-track direction because of the antenna directivity.

and the distributions are entirely due to the actual lightning processes. In Figure 12b, the distributions are plotted in a linear-logarithmic format. Both follow the same linear decline in Figure 12b, showing that both have the same exponential distribution, in terms of density distribution,

$$p(x_E) = \frac{n(x_E)}{N} = \frac{1}{a} e^{-x_E/a} \tag{9}$$

Here, N is the total number of the naturally occurring events regardless of the FORTE detection, a is the falloff rate of the distribution, x_E is the radiation amplitude that spans from 0 to ∞, and n is the number of events at x_E.

[40] Notice that Figure 12b shows the grand distributions for all the events across the 90° zenith angles for the two separate groups, and no directivity was concerned. Equation (9) would be valid if the radiation had an isotropic beam pattern, or if the polarized discharges were probed from a fixed direction. For radiation that is not isotropic, and if the probing direction is not fixed, the distribution can be expressed as

$$p(x_E, \theta) = \frac{n(x_E, \theta)}{N} = \frac{1}{ab(\theta)} e^{-\frac{x_E}{ab(\theta)}} \tag{10}$$

where $b(\theta)$ represents the source beam pattern. Equation (10) can be interpreted with the help of Figure 13. In Figure 13a, three emitters are assumed to sit at the same location and to be vertical. They have identical radiation pattern but have different intensities, and the intensities follow an exponential relation. If one views the emitters along θ_1 an exponential amplitude distribution like that shown in Figure 13b would be obtained (but with only 3 points on the curve). Viewing from another angle θ_2 would yield another exponential curve on which the three corresponding points would shift leftward to smaller amplitudes. The area integrals below the two curves will be the same, equal to the total number of emitters.

[41] Equation (10) can be used directly when the observers are all at the same distance from the emitters and the observers are equipped with identical VHF antennas. With the FORTE observations, the lightning-satellite distance $d(\theta)$ will change, and the receiving antenna has its own directivity $g(\theta)$. Under these considerations and through similar arguments as that for equation (10), the effective amplitude distribution can be written as

$$p(x_E, \theta) = \frac{n(x_E, \theta)}{N} = \frac{d(\theta)/H}{ab(\theta)g(\theta)} e^{-\frac{x_E d(\theta)/H}{ab(\theta)g(\theta)}} \tag{11}$$

where H is the altitude of the orbit, which represents the shortest discharge-satellite distance, and is used as a reference distance.

[42] Finally, the number of the events that would be detected by the FORTE satellite at each zenith angle depends also on the trigger threshold $X_T(\theta)$, which itself is a function of θ. The event density, or equivalently the detection probability for a single event, can be expressed as

$$\frac{\overline{N}(\theta)}{N} = \int_{X_T(\theta)}^{\infty} \frac{d(\theta)/H}{ab(\theta)g(\theta)} e^{-\frac{x_E d(\theta)/H}{ab(\theta)g(\theta)}} dx_E = e^{-\frac{X_T(\theta) d(\theta)/H}{ab(\theta)g(\theta)}} \tag{12}$$

Here, $\overline{N}(\theta)$ is the total number of events above the threshold, or being selected in case of narrow-burst events, at zenith angle θ. On the basis of equation (12), we see that if $X_T(\theta)$ were zero, we would have $\overline{N}(\theta)/N = 1$; that is, all the events would be detected at this angle. If $X_T(\theta)$ was zero across the entire zenith range, the detection probability across θ would be uniformly 1.

[43] We now consider further the effects of the trigger threshold on the detection probability. As indicated by equation (12), it would be ideal if the trigger threshold were a unique function of the zenith angle. Because of the behavior of the trigger system and the nature of the observation, the inferred threshold displays a range of uncertainty, as shown in Figure 9. Fortunately, this appears not to be a problem for our study. At a given zenith angle, the variations of the threshold closely resemble a random process. Around their mean value, there are likely equal numbers of points below and above. Putting this statistical feature into equation (12), it is straightforward to find that by using a mean threshold for the lower integration limit we would exclude the events that were associated with lower thresholds, but at the same time we would add extra events that were associated with higher thresholds. The likely result is that the two factors roughly compensate each other, and the integrated number of events would not change.

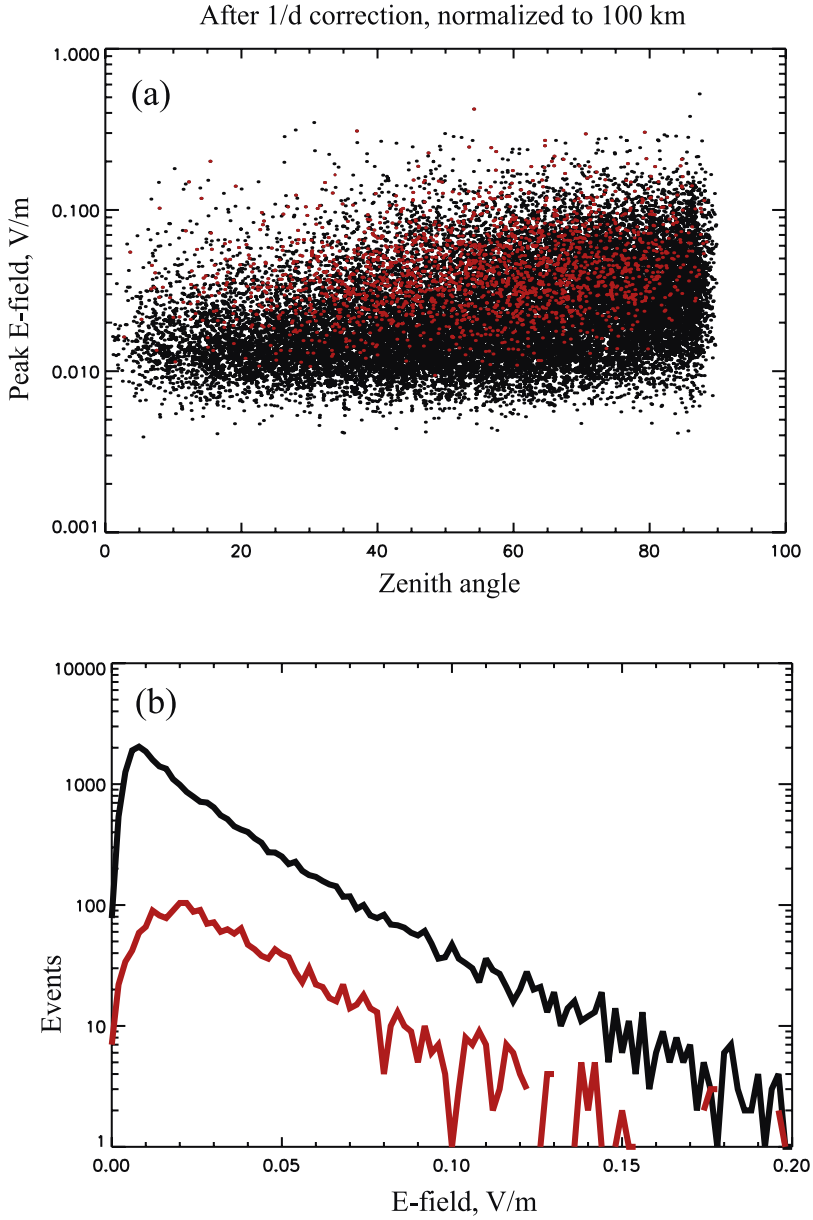

Figure 12. (a) Peak *E* fields normalized to 100 km for the overall events (black) and the narrow bursts (red). (b) *E* field amplitude distributions for the two groups.

[44] Nevertheless, the selection process for the narrow-burst events was less capable of picking out the week bursts, and therefore effectively raised the threshold for such events. It is difficult to accurately determine the resultant threshold on the basis of Figure 12, but it can be seen that it is not significantly greater than the threshold for the overall events. Later analysis in section 4.6 suggests that the threshold was effectively elevated by a factor of 0.2.

[45] In the following analysis, the same threshold relation $(d/H)^{-0.42}$ will be used for both groups except that a factor of 1.2 will apply to the narrow bursts. Thus, in equation (12), the left-hand side represents the event density distribution, and the right-hand side contains the source beam pattern $b(\theta)$ and other parameters. Among these, $X_T(\theta)$ and $g(\theta)$ have just been discussed, H is known (800 km), $d(\theta)$ follows equation (4), and a is falloff rate for the amplitude distribution (Figure 12b).

4.6. Observation and Model Comparisons

[46] Having discussed all the relevant parameters and established the relation between the beam pattern and the event density distribution, we are now ready to compare the observed distributions (Figure 8) with the predictions of equation (12). In Figure 14, the solid line is the observation for all the coincident events, the same as in Figure 8. The dashed line is the simulated result based on equation (12). In the simulation an isotropic lightning radiation beam pattern, $b(\theta) = 1$ is assumed. Both curves are normalized to their own maximums for comparison. In the simulation, all the angle-independent constants are combined into a single constant. For the overall events, the constant was deter-

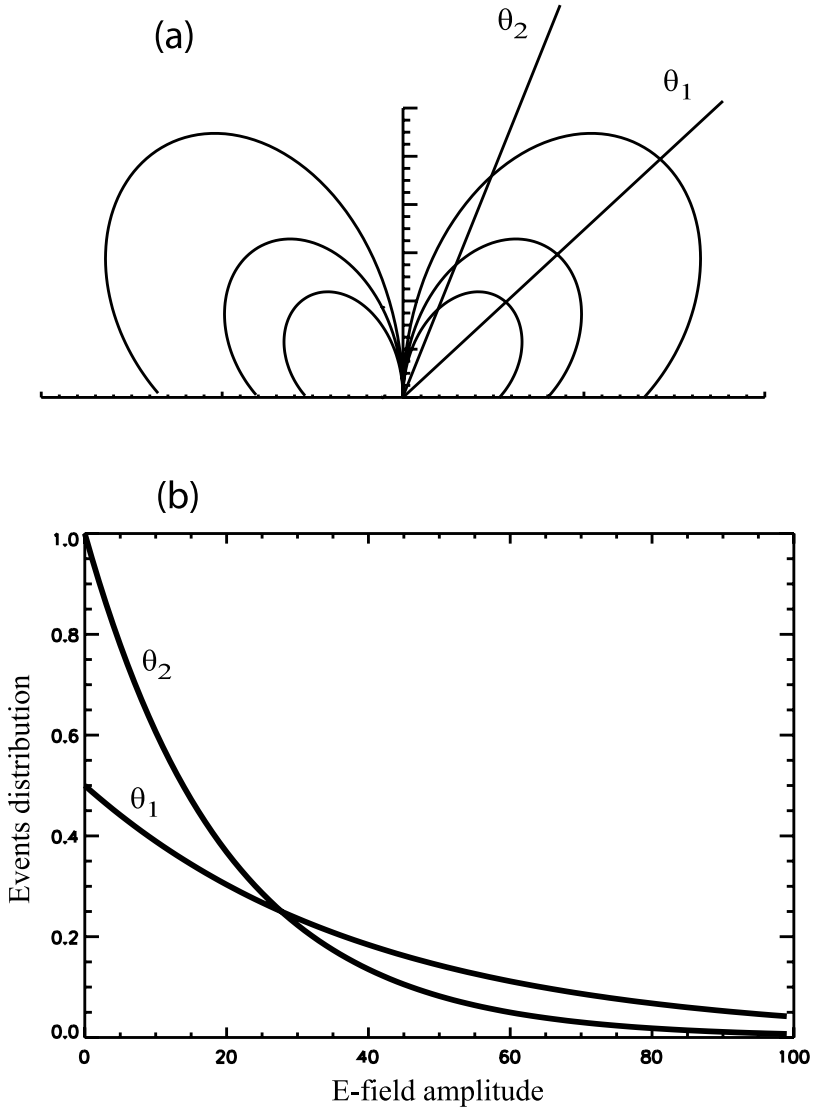

Figure 13. Relations between (a) the radiation beam pattern and (b) the angularly dependent amplitude distributions at the two zenith angles indicated.

mined 3.15. It is clear from Figure 14 that the two curves agree with each other very well, indicating that the ensemble of all the coincident events can be considered to have an isotropic pattern. This is statistically valid, and is not to say that each individual event is an isotropic emitter. The isotropic pattern for the overall events is consistent with the fact that the vast majority of the events are unpolarized, or randomly oriented.

[47] Figure 15 compares the observed event density distribution for the narrow bursts (solid curve) with the model simulations based on the (1) dipole model (dot-dashed curve), (2) free-space traveling current model (dashed curve), and (3) on-ground traveling current model (dotted curve), respectively. For this group the combined constant was 1.2×3.15. The factor of 1.2 is used to accommodate the effective threshold elevation for the narrow bursts. The rest of the simulations are the same as that for the isotropic model, except that $b(\theta)$ in equation (12) is replaced respectively by the three beam patterns showed in Figure 1 by the dashed curves. The speed of the current wave is assumed 0.75c for the two traveling current models. Clearly, a dipole radiation model for the narrow bursts does not agree with that observed. For the on-ground traveling current model, there appears to be some agreement at zenith angles less than 40° but not at greater zenith angles. It is obvious that the free-space traveling current model gives the best agreement.

[48] To obtain the best fit between the observation and the traveling current models, different traveling speeds were tried. We found that $0.75c$ gives the best results for both the traveling current models. It should be pointed out that the dashed curves in Figure 1, that simulated beam patterns for statistically vertical discharges but not for purely vertical discharges, were used for the respective $b(\theta)$. Without overcrowding Figure 15, we note that with the pure vertical models, the simulated event density distributions are much the same as that presented in Figure 15, except some slight differences in the zenith angles 0–15°. This would be expected from the comparisons in Figure 1.

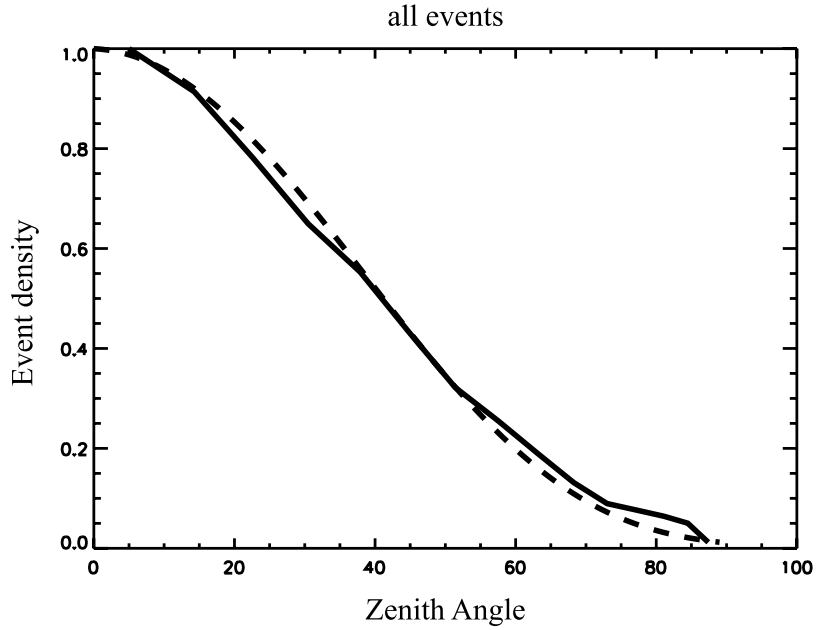

Figure 14. Comparing the event density distributions between the overall events (solid) and the model simulation (dashed, equation (12)). An isotropic model $b(\theta) = 1$ is used for the simulation.

[49] On the basis of event density distributions, we can conclude that the overall parent events follow an isotropic beam pattern as a group. If this is true, the explicit beam pattern for the narrow bursts can be obtained by comparing its event density distribution to that of the overall events. To do this we first normalize each of the two distribution curves (Figure 8) with the areas under the curves, respectively, such that each is normalized to a total of one event. Such normalized distributions are equivalent to the detection probabilities, as a function of the viewing angle. On the basis of equation (12) and the fact of that the observational parameters are common to the two distributions (except the effective thresholds for the two groups), we have, by assuming $b_{all}(\theta) = 1$,

$$\frac{\ln\left(\overline{N}(\theta)/N\right)|_{all}}{\ln\left(\overline{N}(\theta)/N\right)|_{narrow}} = \frac{\left(-\frac{X_T(\theta)d(\theta)/H}{ab(\theta)g(\theta)}\right)_{all}}{\left(-\frac{X_T(\theta)d(\theta)/H}{ab(\theta)g(\theta)}\right)_{narrow}} = \frac{X_{T\_all}(\theta)}{X_{T\_narrow}(\theta)}\,\frac{b_{narrow}(\theta)}{b_{all}(\theta)} = \frac{X_{T\_all}(\theta)}{X_{T\_narrow}(\theta)}\,b_{narrow}(\theta) \tag{13}$$

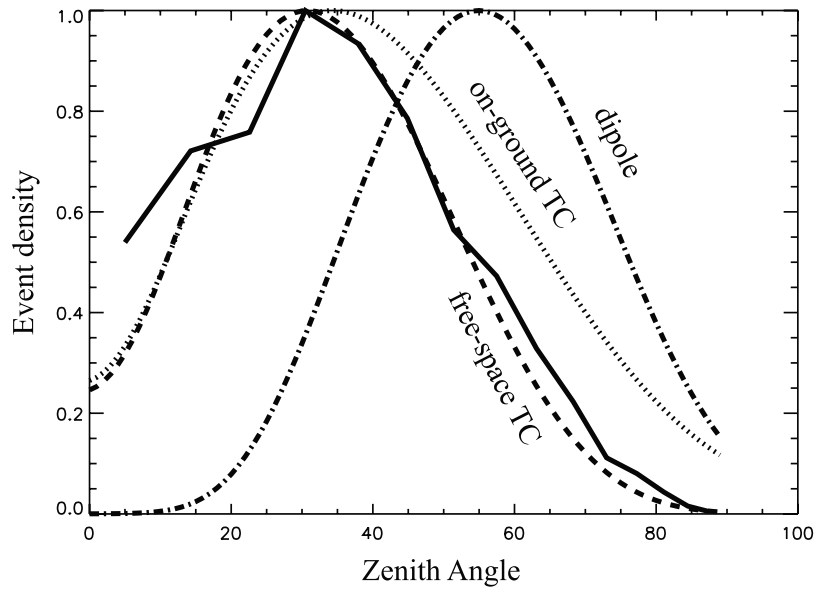

Figure 15. Comparing the event density distributions between the narrow bursts (solid) and the model simulations of a dipole (dot-dashed), a free-space traveling current (dashed), and an on-ground traveling current (dotted). A statistical direction deviation of $\sigma(\theta) = 12°$ from vertical ($\bar{\theta} = 0$) is used for the simulations. The speed v is assumed 0.75c for the two latter models.

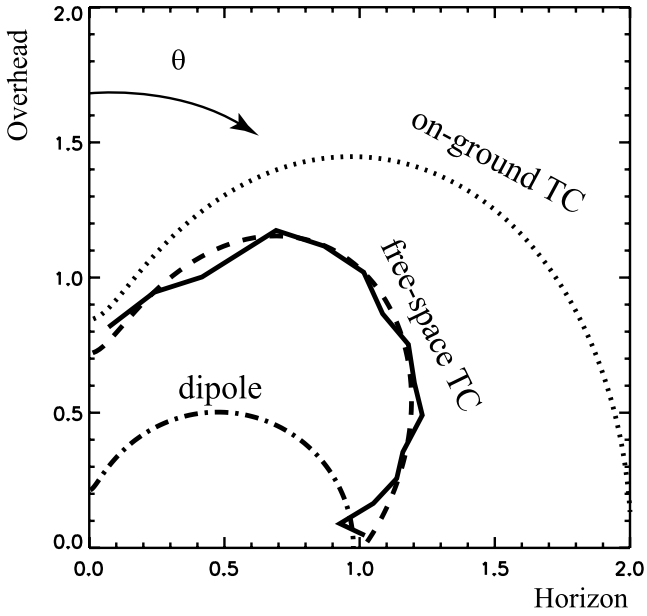

Figure 16. Direct beam pattern comparisons between that of the narrow bursts and the three different models (Figure 1). The former is inferred by comparing the event density distributions between the narrow bursts and the overall events, according to equation (13).

The advantage of this equation is that almost all the instrumental and observational parameters are removed, so that no special considerations are needed for the antenna response, lightning-satellite distance, and actual distribution of lighting radiation amplitude.

[50] In Figure 16 the solid curve shows the ratio of the left-hand side multiplied by a factor of 1.2, and is compared with the three beam patterns shown in Figure 1. The result is presented in a polar format with the zenith pointing upward and the horizon pointing to the right, the same as in Figure 1 but with only one quadrant. Again, it is clear that the inferred beam pattern for the narrow bursts agrees very well with the free-space traveling current model, but not as well with the other two models. The speed of the current wave was again assumed 0.75c. The factor 1.2 represents the ratio of X_{T_narrow}/X_{T_all} due to the effectively higher threshold for the narrow bursts. The value of 1.2 is found to be the best fit for the comparisons, and as can be seen in Figure 16, other factors will not yield better agreement with the modeled beam pattern. The 0.2 increase of the narrow bursts threshold is also in general agreement with what indicated in Figure 12b, in which only slight difference can be seen near the peak areas. The same 1.2 factor that was used earlier in equation (10) for the narrow-burst analysis (Figure 15) is based on the discussion here. For the dipole and the on-ground traveling current models, no proper factor can ever be found to fit them, as shown by the dissimilar shapes between the solid curve and the two modeled curves. In this analysis, the ratio of X_{T_narrow}/X_{T_all} is assumed independent of zenith angle θ. Although they are separately dependent on θ, statistically they should have the same downward trend as θ increases.

5. Discussion

[51] In this paper, we have analyzed the possible VHF radiation beam patterns for the FORTE/NLDN coincident events through careful statistical analyses based on the FORTE observed event density distributions. We treated the overall parent events as one group (25,721), and extracted the very narrow bursts (<100 ns) that are associated with the initiation of return strokes as another group (2092). It was found that the ensemble of the overall events showed a near-isotropic radiation pattern (Figure 14), and that the ensemble of the narrow bursts showed a pattern that agrees with that of a free-space traveling current pulse at the speed of 0.75c (Figure 15). Comparing the event density distributions between the two groups shows an explicit beam pattern for the narrow bursts, which again agrees well with that of the 0.75c free-space traveling current pulse (Figure 16).

[52] In the work by *Jacobson and Shao* [2002], we reviewed ground observations of return strokes that reported fast electric field (E) transient with a risetime <100 ns, narrow *E* field derivative (dE/dt) and narrow current derivative (dI/dt) pulse with a pulse width <100 ns. For natural lightning, these were mostly obtained for seawater strokes when the E and dE/dt sensors were set up at the Florida coastline [e.g., *Weidman and Krider*, 1980; *Le Vine et al.*, 1989; *Krider and Leteinturier*, 1996; *Willett et al.*, 1998; *Willett and Krider*, 2000]. Observations like this avoided the land path that would selectively attenuate the high-frequency portion of the signal. We also noticed that for triggered lightning return strokes similar fast transient/narrow pulses were reported [e.g., *Le Vine et al.*, 1989; *Leteinturier and Eybert-Berard*, 1991; *Uman et al.*, 2000; *Schoene et al.*, 2003]. The ground-based E and dE/dt measurements are typically conducted in the LF-HF (<30 MHz) range, whereas the FORTE observations presented in this study are at the lower end of VHF (26–48 MHz), and the temporal signatures between the two may not directly comparable. However, the two types of measurement have a similar bandwidth and will yield a similar time response. The compatible pulse/burst width between FORTE and ground observations suggests FORTE's narrow bursts are related to these ground-based fast transient/narrow pulses at the beginning of the return strokes. Furthermore, given the narrow burst's tight temporal correlation (<10 μs, limited by FORTE's position and timing accuracy) with the NLDN stroke time [*Jacobson and Shao*, 2002], and the fact that it is the most powerful radiation in the 164 μs time interval, it is not likely associated with other discharge processes but rather with the most intense and fast transient of the return stroke process.

[53] Nevertheless, *Willett et al*. [1990] and *Willett and Krider* [2000] reported that stepped leader pulses, dart-stepped leader pulses, and certain intracloud pulses also show similar narrow width with −CG initiation transients, but they are somewhat weaker than the −CG transients [*Willett et al*., 1990]. *Heidler and Hopf* [1998] reported dE/dt pulse widths of ½ μs or more with ½ μs scatter for

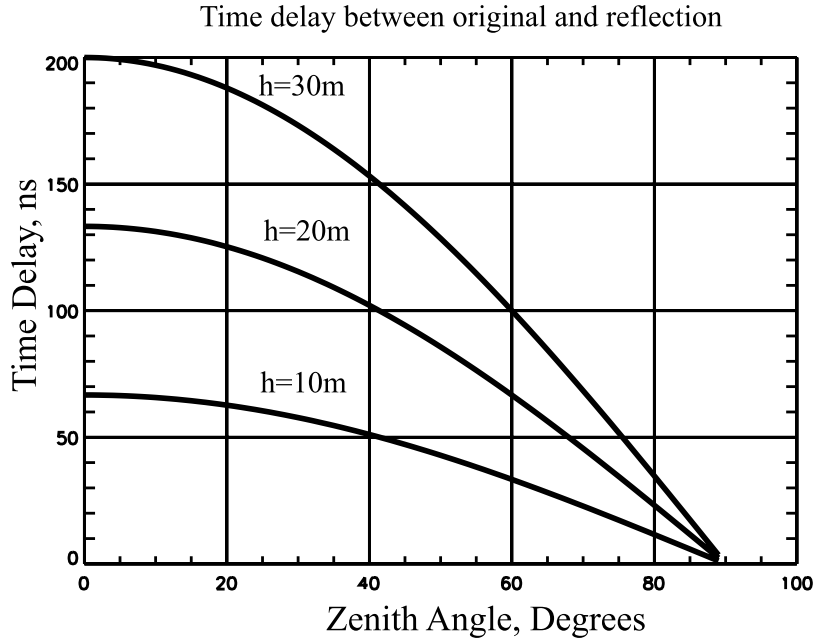

Figure 17. Time delay between the original and the reflected burst at the satellite.

natural return strokes over land. Even though the signals propagated over lossy land, they argued that the wide scatter in the widths could not be accounted for by propagation effects. Instead, *Willett et al.* [1998] speculated that this may be due to real broadening at the source as compared to seawater return stroke pulses. By contrast, *Uman et al.* [2000] did not observe significant broadening from overland triggered return strokes. This issue is as yet unresolved.

[54] In this paper, the speed of the current pulse responsible for the narrow VHF bursts is inferred as $0.75c$, appearing to be slightly higher than what has been reported before from ground-based measurements [e.g., *Idone and Orville*, 1982; *Willett et al.*, 1988, 1989; *Schoene et al.*, 2003]. Using a TL model for triggered lightning, *Willett et al.* [1988, 1989] from the radiation field at 5.16 km and *Schoene et al.* [2003] from the total field at 15 m and 30 m, estimated the same speed of $\sim 2/3c$ after comparing the current derivative and the field derivative, and $\sim 1/2c$ after comparing the current and the field. It is conceivable that these two different speeds indicate a decrease of propagation speed after the initiation of the return stroke [*Schoene et al.*, 2003]. A speed as high as c was reported for triggered lightning by *Leteinturier et al.* [1990] and *Uman et al.* [2000] from peak current derivative and nearby (10s m) peak E field derivative, but this was overestimated because of an assumption that the radiation field dominates the field derivative at the initial stage of the return stroke, as discussed by *Uman et al.* [2000, 2002] and *Schoene et al.* [2003]. Nevertheless *Wang et al.* [1999] from high-speed optical imagery reported a speed $\sim c$ for one of two triggered lightning strokes they studied. The other one had a speed of 2/3c. It was noted that even though triggered lightning is similar to natural lightning, they are clearly not identical. A natural initial stroke has no direct analogy to triggered lightning.

[55] The fact that only a small number, seawater-preferred stokes display the distinctive narrow VHF burst in the FORTE data set suggests that they belong to a small outlying group of higher speed and more intense return strokes. The other strokes in the parent group appear to be "normal" (Figures 4a and 4b) and they may be associated with the "normal" return stroke speed and intensity. Unfortunately, the present study is unable to resolve this issue.

[56] It is interesting to note that the inferred pattern agrees very well with a free-space model but not nearly as well with the on-ground model (Figures 15 and 16). This suggests that the source of the narrow VHF radiation was above the surface of the Earth. For a narrow VHF burst above the Earth surface, the ground serves as a reflector for FORTE. The surface-reflected burst will be delayed in time, and in general will not add to the original burst either in time or in phase. For instance, if the source is at 20 m, to an overhead observer, the reflected burst arrives 133 ns later, entirely separate from the original burst of <100 ns wide. Figure 17 shows the time delays between the original and the reflected bursts as a function of zenith angle, for three different heights (10, 20, and 30 m). For the present study, FORTE has a bandwidth B of 22 MHz and the intrinsic coherent time between the two bursts is about 1/B, 45 ns [*Shao et al.*, 2004]. To treat the surface as a time-independent mirror (equation (2)), Figure 17 suggests that the source would have to be within a few meters above the surface, if not right on the surface. On the other hand, for the reflected burst separating from the original burst (to agree with the free-space model), the source needs to be high enough so that the time delay between them would exceed the half-width of the burst. As shown in Figure 17, for burst width <100 ns, a 20–30 m height appears to satisfy this latter requirement at most of the zenith angles.

[57] One may argue that if the source is high enough, the reflected burst should be separately detected, against the single-burst phenomenon presented in this paper. This would be true if the radiation were not highly upward

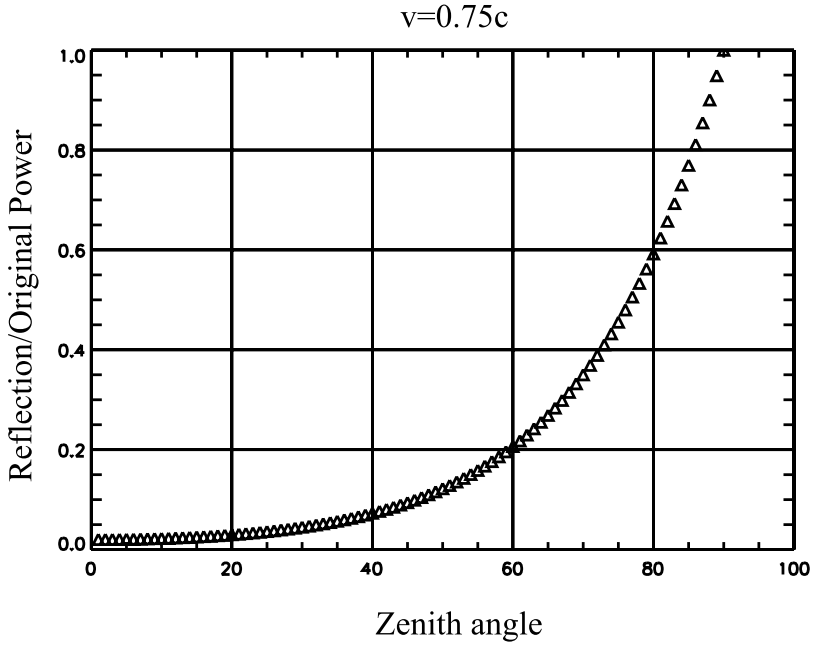

Figure 18. Power ratio of the reflection to the original, for $v = 0.75c$ free-space traveling current radiation.

directed. For an upward traveling current pulse, the reflected radiation power could be a small fraction of the original power, especially at small zenith angles, as shown in Figure 18 for a traveling speed of $0.75c$. It shows that from 0° to 70°, the reflected power is less than $1/e$ of the original power (reflection coefficient is assumed 1). This makes the reflected burst less visible at most viewing angles. Only near to the horizon, the reflected power approaches the level of the original power, but at the same time the temporal separation decreases between the pair (Figure 17), such that it is difficult to distinguish the two bursts sequentially. Therefore, in either case the reflected burst is less likely to be clearly detected. To see the reflected burst, the source would have had to be much higher than 20–30 m, i.e., a few 100s of meters; and because of the radiation beam pattern, it could only be seen at zenith angles greater than ~70°.

[58] On the basis of the above discussion, the source height of the narrow bursts is likely to be a few tens of meters above the surface of the Earth. It is unlikely the sources would be much higher, since (1) these bursts are associated with the very beginning of the return strokes and (2) no distinguishable reflection has been observed. Indeed, these bursts appear to be closely associated with the attachment process of the return strokes. As reviewed by *Uman* [1987], the junction point of the attachment process has been reported to be 10–50 m above the ground by many researchers, although the review was limited to initial strokes. Recently, *Wang et al.* [1999] reported direct observations of the attachment process in two triggered lightning strokes that were started by dart leaders, similar to the subsequent strokes in natural −CGs. They found that the junction points were several to eleven meters above the tip of a grounded metallic rod, which itself was 4 m tall. On the basis of lower–time resolution streak camera observations, *Idone* [1990] inferred that the height of the dart leader/return stroke junction point was in the range 12–27 m. Apparently, the height we inferred in this study agrees with the heights of the junction point reported by these researchers.

[59] In this paper, we compared the observations with the beam pattern of an upward propagating current pulse (e.g., equation (1)). As discussed by *Shao et al.* [2004, 2005], such a discharge model is equivalent to the TL model if the current does not change its shape and propagates at a constant speed. In this case, $\partial i(z', t')/\partial t' = 0$ everywhere except at the source point, so that the radiation is solely produced from the current source location. In the present study, the traveling velocity is assumed constant, and for a single current pulse the model is identical to the TL model.

[60] If the current decays while it propagates forward (a modified TL model, MTL), the beam pattern will be modified from the TL model, and the degree of the modification depends on the velocity, the rate of the current decay, the current pulse shape, and the time at which the radiation is observed, as indicated by equation (11) of *Shao et al.* [2005]. Comparing FORTE observation to the MTL radiation is out of the scope of this paper, because of the large number of unknown variables.

[61] For a traveling current source (TCS) model [*Heidler*, 1986], the upward extending wave front (at speed v) instantaneously triggers the current source along the channel, and the triggered current travels downward at speed c into the ground. If the initiation point is assumed 20–30 m high, the current absorption at the ground is delayed long enough so that its radiation should not affect the initial radiation burst. In this case, the initial radiation is produced by a bidirectional current wave, similar to the case of equation (2), except that the up and downward speeds are v and c. It is evident that if v nears c (for instance $v > 0.5c$) one would expect a beam pattern similar to equation (2) (but not to (1)) in the upper half-space. In the lower half-space, the radiation would be significantly enhanced in the down-

ward direction. As discussed above, the beam pattern described by equation (2) is not observed in the upper half-space, suggesting that the TCS model is not suitable for the initiation of the return stroke. Ground-based observations of nearby triggered lightning by *Schoene et al.* [2003] with total (not only radiation) field also suggested that the TCS model is less suitable than the TL model in the initial microsecond of the return stroke.

[62] As speculated by some investigators [e.g., *Uman et al.*, 1973; *Weidman and Krider*, 1978; *Idone et al.*, 1984; *Weidman et al.*, 1986; *Willett et al.*, 1988; *Leteinturier et al.*, 1990] and documented by *Wang et al.* [1999] with optical measurement, a return stroke is likely to start with two current waves at the junction point that propagate simultaneously upward and downward, similar to the TCS model at the very initial stage. Unfortunately, little is known about the characteristics of the downward wave. Analogous to the discussion on the TCS model, if the two current waves have the same amplitude and speed, the beam pattern is expected to be the same as equation (2) (Figure 1). Again, our observation agrees with a single upward current pulse instead, but not with the bidirectional current concept. One could suggest that if the downward current were much weaker than the upward current, its contribution to the radiation field would be negligible. Or, one may speculate the seawater attachment process (upward leader, bidirectional current) is different than the land stroke. To resolve this issue, further studies regarding the details of the bidirectional junction process are needed.

[63] Finally, with the burst width τ and the propagating speed v, we can roughly estimate the physical size of the moving current pulse. If the concept of the TL model is used, the length of the current pulse will be $\sim v\tau$. Since the bursts are narrower than 100 ns and the speed is inferred as 0.75c, the physical size of the corresponding sources will not be longer than $\sim$20 m.

Appendix A: VHF Transionospheric Phase Delay

[64] Starting from the Appleton-Lassen equation [*Budden*, 1985, p. 74] and assuming the signal frequencies well above the plasma, collision, and electron cyclotron frequencies (justified for VHF signals), the ionospheric refractive index μ can be approximated as [*Davies*, 1990, p.77]

$$\mu^2 = 1 - \frac{f_p^2}{f^2(1 \pm f_L/f)} \tag{A1}$$

under the quasilongitudinal (QL), approximation. Here, $f_p \equiv \sqrt{e^2 n/2\pi\varepsilon_0 m_e}$ is the plasma frequency, where n is the electron density; f is the signal frequency; $f_L = f_c \cos\gamma$, where $f_c \equiv 2\pi eB/m_e$ is the electron cyclotron frequency, and γ is the angle between **k** (wave vector) and **B** (magnetic field) which should not be very close to a right angle for the QL approximation. Since $f_p \ll f$ and $f_L \ll f$, μ can be expended in terms of $1/f$

$$\mu = 1 - \frac{1}{2}\frac{f_p^2}{f^2(1 \pm f_L/f)} + \mathrm{O}\left(\frac{f_p}{f}\right)^4 + \ldots \tag{A2}$$

and higher-order terms can be neglected.

[65] The phase of the signal changes by $d\varphi_{free\_space} = 2\pi f dx/c$ in free space and $d\varphi_{ionosphere} = 2\pi f\mu dx/c$ in the ionosphere as it progresses forward dx. The total phase difference between the two media along the lightning-satellite line of sight can be expressed as

$$\int \left(d\varphi_{free\_space} - d\varphi_{ionosphere}\right) = \frac{e^2}{2c\varepsilon_0 m_e}\frac{1}{(f \pm f_L)}\int n dx \tag{A3}$$

where, f_L is approximated with the value at the interception point between **k** and the ionospheric layer, and the integral at the right-hand side is the total electron content (TEC) along the line of sight.

[66] **Acknowledgments.** We thank Phil Klingner for his help on retrieving the FORTE trigger threshold. We also want to thank the reviewers for their constructive and stimulating comments which significantly improved this paper. We are grateful to John Willett for encouraging us to submit this paper to JGR. This work was performed at the Los Alamos National Laboratory under the auspices of the U.S. Department of Energy.

References

Budden, K. G. (1985), *The Propagation of Radio Waves*, Cambridge Univ. Press, New York.

Cummins, K. L., M. J. Murphy, E. A. Bardo, W. L. Hiscox, R. Pyle, and A. E. Pifer (1998), Combined TOA/MDF technology upgrade of U.S. National Lightning Detection Network, *J. Geophys., Res.*, *103*, 9035–9044.

Davies, K. (1990), *Ionospheric Radio*, Peter Peregrinus, London.

Heidler, F. (1986), Some deductions from the traveling current source model, paper presented at the 6th International Zurich Symposium on Electromagnetic Compatibility, Inst. Of Telecommun., Wroclaw, Poland.

Heidler, F., and C. Hopf (1998), Measurement results of the electric fields in cloud-to-ground lightning in nearby Munich Germany, *IEEE Trans. Electromagn. Compat.*, *40*(4), 436–443.

Idone, V. P. (1990), Length bounds for connecting discharges in triggered lightning subsequent strokes, *J. Geophys. Res.*, *95*, 20,409–20,416.

Idone, V. P., and R. E. Orville (1982), Lightning return stroke velocities in the Thunderstorm Research International Program (TRIP), *J. Geophys. Res.*, *87*, 4903–4915.

Idone, V. P., R. E. Orville, P. Hubert, L. Barret, and A. Eybert-Berard (1984), Correlated observations of three triggered lightning flashes, *J. Geophys. Res.*, *89*, 1385–1394.

Jacobson, A. R., and X. M. Shao (2002), FORTE satellite observations of very narrow radiofrequency pulse associated with the initiation of negative cloud-to-ground lightning stroke, *J. Geophys. Res.*, *107*(D22), 4661, doi:10.1029/2001JD001542.

Jacobson, A. R., S. O. Knox, R. Franz, and D. C. Enemark (1999), FORTE observations of lightning radio-frequency signatures: Capabilities and basic results, *Radio Sci.*, *34*, 337–354.

Jacobson, A. R., K. L. Commins, M. Carter, P. Klingner, D. Roussel-Dupre, and S. O. Knox (2000), FORTE radio-frequency observations of lightning strokes detected by the National Lightning Detection Network, *J. Geophys. Res.*, *105*, 15,653–15,662.

Krider, E. P. (1992), On the electromagnetic fields, Poynting vectors, and peak power radiated by lightning return strokes, *J. Geophys. Res.*, *97*, 15,913–15,917.

Krider, E. P., and C. Leteinturier (1996), Submicrosecond fields radiated during the onset of first return strokes in cloud-to-ground lightning, *J. Geophys. Res.*, *101*, 1589–1597.

Langel, R. A. (1992), International Geomagnetic Reference Field: The 6th generation, *J. Geomagn. Geoelectr.*, *44*(9), 679–707.

Leteinturier, C., and A. Eybert-Berard (1991), Submicrosecond characteristics of lightning return stroke currents, *IEEE Trans. Electromagn. Compat.*, *33*(4), 351–357.

Leteinturier, C., C. Weidman, and J. Hamelin (1990), Current and electric field derivatives in triggered lighting return strokes, *J. Geophys. Res.*, *95*, 811–828.

Le Vine, D. M., and J. C. Willett (1992), Comment on the transmission line model for computing radiation from lightning, *J. Geophys. Res.*, *97*, 2601–2610.

Le Vine, D. M., J. C. Willett, and J. C. Bailey (1989), Comparison of fast electric field changes from subsequent return strokes of natural and triggered lightning, *J. Geophys. Res.*, *94*, 13,259–13,265.

Massey, R. S., S. O. Knox, R. C. Franz, D. N. Holden, and C. T. Rhodes (1998), Measurements of transionospheric radio propagation parameters using the FORTE satellite, *Radio Sci.*, *33*(6), 1739–1753.

Rhodes, C. T., X. M. Shao, P. R. Krehbiel, R. J. Thomas, and C. O. Hayenga (1994), Observations of lightning phenomena using radio interferometry, *J. Geophys. Res.*, *99*, 13,059–13,082.

Schoene, J., M. A. Uman, V. A. Rakov, K. J. Rambo, J. Jerauld, and G. H. Schnetzer (2003), Test of the transmission line model and the traveling current source model with triggered lightning return strokes at very close range, *J. Geophys. Res.*, *108*(D23), 4737, doi:10.1029/2003JD003683.

Shao, X. M., and A. R. Jacobson (2001), Polarization observations of broadband VHF signals by the FORTE satellite, *Radio Sci.*, *36*, 1573–1589.

Shao, X. M., and A. R. Jacobson (2002), Polarization observations of lightning-produced VHF emissions by the FORTE satellite, *J. Geophys. Res.*, *107*(D20), 4430, doi:10.1029/2001JD001018.

Shao, X. M., P. R. Krehbiel, R. J. Thomas, and W. Rison (1995), Radio interferometric observations of cloud-to-ground lightning phenomena in Florida, *J. Geophys. Res.*, *100*, 2749–2783.

Shao, X. M., D. N. Holden, and C. T. Rhodes (1996), Broad band radio interferometry for lightning observations, *Geophys. Res. Lett.*, *23*, 1917–1920.

Shao, X. M., C. T. Rhodes, and D. N. Holden (1999), RF radiation observations of positive cloud-to-ground flashes, *J. Geophys. Res.*, *104*, 9601–9608.

Shao, X. M., A. R. Jacobson, and T. J. Fitzgerald (2004), Radio frequency radiation beam pattern of lightning return strokes: A revisit to theoretical analysis, *J. Geophys. Res.*, *109*, D19108, doi:10.1029/2004JD004612.

Shao, X. M., T. J. Fitzgerald, and A. R. Jacobson (2005), Reply to comment by R. Thottappillil and V. A. Rakov on "Radio frequency radiation beam pattern of return strokes: A revisit to theoretical analysis," *J. Geophys. Res.*, doi:10.1029/2005JD005889, in press.

Stearns, S. D., and D. R. Hush (1990), *Digital Signal Analysis*, Prentice-Hall, Upper Saddle River, N. J.

Suszcynsky, D. M., M. W. Kirkland, A. R. Jacobson, R. C. Franz, S. O. Knox, J. L. L. Guillen, and J. L. Green (2000), FORTE observations of simultaneous VHF and optical emissions from lightning: Basic phenomenology, *J. Geophys. Res.*, *105*, 2191–2201.

Thottappillil, R., M. A. Uman, and V. R. Rakov (1998), Treatment of retardation effects in calculating the radiated electromagnetic fields from the lightning discharge, *J. Geophys. Res.*, *103*, 9003–9013.

Uman, M. A. (1987), *The Lightning Discharge*, Elsevier, New York.

Uman, M. A., and D. K. McLain (1969), Magnetic field of lightning return strokes, *J. Geophys. Res.*, *74*, 6899–6910.

Uman, M. A., D. K. McLain, R. J. Fisher, and E. P. Krider (1973), Currents in Florida lightning return strokes, *J. Geophys. Res.*, *78*, 3530–3537.

Uman, M. A., V. A. Rakov, K. J. Schnetzer, K. J. Rambo, D. E. Crawford, and R. J. Fisher (2000), Time derivative of the electric field 10, 14, and 30 m from triggered lightning strokes, *J. Geophys. Res.*, *105*, 15,577–15,595.

Uman, M. A., J. Schoene, V. A. Rakov, K. J. Rambo, and G. H. Schnetzer (2002), Correlated time derivatives of current, electric field intensity, and magnetic flux density for triggered lightning at 15 m, *J. Geophys. Res.*, *107*(D13), 4160, doi:10.1029/2000JD000249.

Wang, D., V. A. Rakov, M. A. Uman, N. Takagi, T. Watanabe, D. E. Crawford, K. J. Rambo, G. H. Schnetzer, R. J. Fisher, and Z.-I. Kawasaki (1999), Attachment process in rocket-triggered lightning strokes, *J. Geophys. Res.*, *104*, 2143–3150.

Weidman, C. D., and E. P. Krider (1978), The fine structure of lightning return stroke waveforms, *J. Geophys. Res.*, *83*, 6239–6247.

Weidman, C. D., and E. P. Krider (1980), Submicrosecond risetimes in lightning return-stroke fields, *Geophys. Res. Lett.*, *7*, 955–958.

Weidman, C., J. Hamelin, C. Leteinturier, and L. Nicot (1986), Correlated current-derivative (dI/dt) and electric field derivative (dE/dt) emitted by triggered lightning, paper presented at the International Aerospace and Ground Conference on Lightning and Static Electricity (ICOLSE), Natl. Interagency Coord. Group, Natl. Atmos. Electr. Hazards Prot. Agency, Dayton, Ohio, June.

Willett, J. C., and E. P. Krider (2000), Rise times of impulsive high-current processes in cloud-to-ground lightning, *IEEE Trans. Antennas Propag.*, *48*(9), 1442–1451.

Willett, J. C., V. P. Idone, R. E. Orville, C. Leteinturier, A. Eybert-Berard, L. Barret, and E. P. Krider (1988), An experimental test of the "transmission-line model" of electromagnetic radiation from triggered lightning return strokes, *J. Grophys. Res.*, *93*, 3867–3878.

Willett, J. C., J. C. Bailey, V. P. Idone, A. Eybert-Berard, and L. Barret (1989), Submicrosecond intercomparison of radiation fields and currents in triggered lightning return strokes based on the transmission-line model, *J. Geophys. Res.*, *94*, 13,275–13,286.

Willett, J. C., J. C. Bailey, C. Leteinturier, and E. P. Krider (1990), Lightning electromagnetic radiation field spectra in the interval from 0.2 to 20 MHz, *J. Geophys. Res.*, *95*, 20,367–20,387.

Willett, J. C., E. P. Krider, and C. Leteinturier (1998), Submicrosecond field variations during the onset of first return strokes in cloud-to-ground lightning, *J. Geophys. Res.*, *103*, 9027–9034.

T. J. Fitzgerald, A. R. Jacobson, and X.-M. Shao, Space and Remote Sensing Sciences Group, Los Alamos National Laboratory, Los Alamos, NM 87545, USA. (xshao@lanl.gov)